

Dedicated to Professor SHI Zhongci in honor of his 80th birthday

# A phase model for point spread function estimation in ground-based astronomy

CHAN Raymond Hon-fu<sup>1,\*</sup>, YUAN Xiaoming<sup>2</sup> & ZHANG Wenxing<sup>3</sup>

<sup>1</sup>*Department of Mathematics, The Chinese University of Hong Kong, Hong Kong, P.R. China*

<sup>2</sup>*Department of Mathematics, Hong Kong Baptist University, Kowloon, Hong Kong, P.R. China*

<sup>3</sup>*School of Mathematical Sciences, University of Electronic Science and Technology of China, Chengdu, P.R. China*

*Email: rchan@math.cuhk.edu.hk, xmyuan@hkbu.edu.hk, wxzh1984@126.com*

Received November xx, 2013; accepted January xx, 2013

---

**Abstract** In ground-based astronomy, images of objects in outer space are acquired via ground-based telescopes. However, the imaging system is generally interfered by atmospheric turbulence and hence images so acquired are blurred with unknown point spread function (PSF). To restore the observed images, the abbreviation of wavefront at the telescope's aperture, i.e., the phase, is utilized to derive the PSF. However, the phase is not readily available. Instead its gradients can be collected by wavefront sensors. Thus the usual approach is to use regularization methods to reconstruct high-resolution phase gradients and then use them to recover the phase in high accuracy. Here, we develop a model that reconstructs the phase directly. The proposed model uses the tight frame regularization and it can be solved efficiently by the Douglas-Rachford alternating direction method of multiplier whose convergence has been well established. Numerical results illustrate that our new model is efficient and give more accurate estimation for the PSF.

**Keywords** Point spread function, astronomical imaging, phase model, tight frame, alternating direction method of multipliers

**MSC(2010)** XXXXX, XXXXX

---

**Citation:** Chan R H, Yuan X M, Zhang W X. A phase model for point spread function estimation in ground-based astronomy. SCIENCE CHINA Mathematics. 2013, xx, doi: 10.1007/s11425-xxx-xxxx-x

---

## 1 Introduction

In ground-based astronomy, images of objects in outer space are acquired via ground-based telescopes. However, the imaging system is generally interfered by atmospheric turbulence and the resulting images are usually blurred. The mathematical model of the imaging system in ground-based astronomy is

$$g(x, y) = k(x, y) * f(x, y) + \varepsilon(x, y), \quad (1.1)$$

where  $f(x, y)$  is the true object in outer space;  $g(x, y)$  is its observation by the ground-based telescope;  $k(x, y)$  is the *point spread function* (PSF) caused by the atmospheric turbulence; ‘\*’ is the convolutional operator; and  $\varepsilon(x, y)$  is zero mean white noise. When the PSF  $k$  is known, the problem (1.1), i.e., finding the true  $f$  from the observation  $g$ , is an ill-posed inverse problem arising from the area of image processing and it has been well investigated during the past decades. There are many efficient algorithms for acquiring high quality approximations to the true  $f$  (see e.g., [4, 23] and references therein).

---

\*Corresponding author

However, in ground-based astronomy, the PSF  $k$  is usually unknown as it is influenced by the fickle and irregular atmospheric turbulence. Blind-deconvolution [5, 20] by simultaneously obtaining  $k$  and  $f$  should be a plausible way for this problem. Nevertheless, it usually requires some prior knowledge on  $k$ , e.g., smoothness, symmetry or sparsity, which commonly can not hold for atmospheric blurring. The Fourier optics model [1, 15] is an approach to directly approximate  $k$ . It expresses  $k$  as a function of the incoming wavefronts of light

$$k(x, y) = |\mathcal{F}^{-1} \{ \mathcal{P}(x, y) \exp [\iota \phi(x, y)] \}|^2, \quad (1.2)$$

where  $\mathcal{F}$  denotes the Fourier transform and  $\mathcal{F}^{-1}$  is its inverse;  $\mathcal{P}(x, y)$  is the mirror aperture function of the telescope ( $= 1$  inside the mirror aperture and  $0$  otherwise);  $\iota = \sqrt{-1}$ ;  $\phi(x, y)$  is the *phase* which measures the deviation from the planarity of the wavefront. Typically, the phase  $\phi$  is disturbed (and thus obliquely affects the accuracy of PSF  $k$ ) by atmospheric turbulence which is quantified by *seeing condition*, see [15]. Specifically, the seeing condition is measured by the ratio  $d/r_0$ , where  $d$  is the diameter of the telescope and  $r_0$  is the Fried parameter. Generally, good seeing condition corresponds to  $d/r_0$  with small magnitude (e.g.,  $d/r_0 \lesssim 10$ ) while poor seeing condition corresponds to  $d/r_0$  with large magnitude (e.g.,  $d/r_0 \gtrsim 20$ ).

Practically, the phase  $\phi$  is not readily available, but its horizontal and vertical direction gradients, denoted respectively by  $\mathbf{s}_x$  and  $\mathbf{s}_y$ , can be collected by the wavefront sensor (WFS). The WFS is a device that measures the phase variation caused by atmospheric turbulence. With the phase gradients being collected, the phase  $\phi$  can be derived by solving the following linear inverse problem (see [1, 19, 21])

$$\begin{bmatrix} \mathbf{s}_x \\ \mathbf{s}_y \end{bmatrix} = \begin{bmatrix} D_x \\ D_y \end{bmatrix} \phi, \quad (1.3)$$

where  $D_x, D_y$  are the derivative operators in the horizontal and vertical directions, respectively. Fried geometry [10] and Hudgin geometry [17] are commonly used for defining  $D_x$  and  $D_y$ . The main obstacle in solving (1.3) is that the phase gradients  $\mathbf{s}_x$  and  $\mathbf{s}_y$  are generally collected by WFS under the coarse grid. These low-resolution phase gradients so obtained contain relatively less information, therefore it is difficult to derive an accurate phase  $\phi$ . The inadequacies on the phase  $\phi$  affect the accuracy in estimating the PSF  $k$  and hence in restoring the image  $f$ .

In [18], under the frozen flow hypothesis over the atmospheric turbulence, a technique for reconstructing the high-resolution phase gradients by the multiple frames of low-resolution phase gradients was proposed. Briefly speaking, some frames of low-resolution phase gradients within a short time period are first collected as follows

$$\begin{cases} s_x^i = RW A_i \mathbf{s}_x + \mathbf{n}_x^i, \\ s_y^i = RW A_i \mathbf{s}_y + \mathbf{n}_y^i, \end{cases} \quad i = 1, 2, \dots, m, \quad (1.4)$$

where  $s_x^i$  and  $s_y^i$  are the two sequences of low-resolution phase gradients in horizontal and vertical directions, respectively;  $R \in \mathbb{R}^{l \times n}$  is a down-sampling matrix which transforms high-resolution phase gradients into low-resolution ones;  $W \in \mathbb{R}^{n \times n}$  is an indicator matrix which represents the telescope aperture;  $A_i \in \mathbb{R}^{n \times n}$  is a motion matrix which describes the shift (linear constant velocity or nonlinear velocity) of the phase gradients in the  $i$ -th frame; and  $\mathbf{n}_x^i$  and  $\mathbf{n}_y^i$  are additive white noise. With the low-resolution phase gradients  $s_x^i$  and  $s_y^i$  at different overlapping locations, the high-resolution phase gradients  $\mathbf{s}_x$  and  $\mathbf{s}_y$  can be reconstructed by some fusing techniques. Accordingly, an accurate phase  $\phi$  can be obtained by solving model (1.3), and hence, a more precise PSF  $k$  can be obtained by (1.2). We summarize this procedure of obtaining the PSF  $k$  and restoring  $f$  by the dashed line in Figure 1. We will call this approach *phase-gradient* approach.

Recent work on this topic mainly followed this phase-gradient approach. For example, Jefferies and Hart [18] investigated the linear constant velocity shift on the atmospheric turbulence. Nagy et al. [8, 22] extended that to the case of nonlinear velocity by using the Tikhonov regularization. Since the phase gradients are generally not smooth, Chan et al. [6] employed the  $l^1$ -regularization for both linear constant

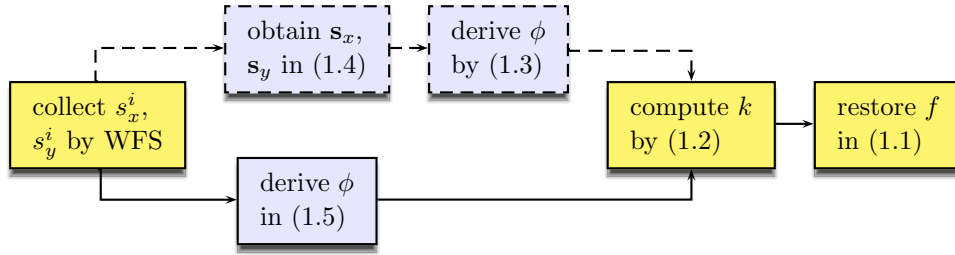


Figure 1. The procedures of imaging system in ground-based astronomy. Dashed line: the phase-gradient approach. Solid line: the phase model.

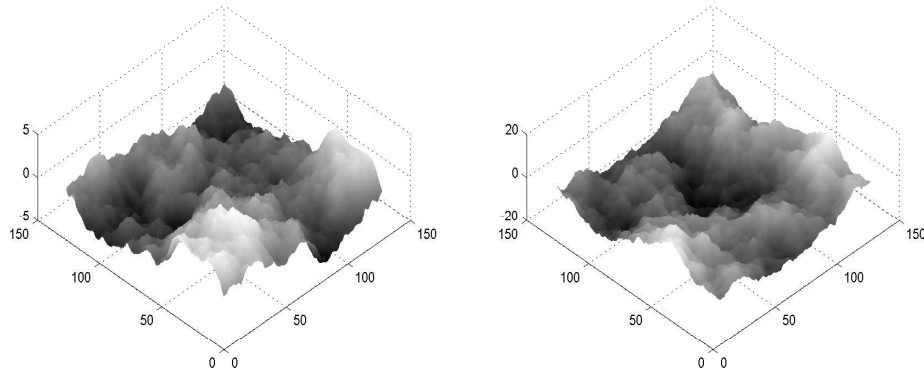


Figure 2. The 3-dimensional surface of 128-by-128 phase. Left: seeing condition  $d/r_0 = 5$ . Right: seeing condition  $d/r_0 = 100$ .

velocity and nonlinear velocity. Numerical results reported therein show that the  $l^1$ -regularization can provide phase gradients with sharper edges and it can be more robust for different possible noises in the measurements.

In this paper, we combine the stages in (1.3)–(1.4), and design a model that computes  $\phi$  directly. Concretely, from (1.3)–(1.4), the low-resolution phase gradients  $s_x^i, s_y^i$  and the phase  $\phi$  are related by

$$\begin{cases} s_x^i = RW A_i D_x \phi + \mathbf{n}_x^i, \\ s_y^i = RW A_i D_y \phi + \mathbf{n}_y^i, \end{cases} \quad i = 1, 2, \dots, m. \quad (1.5)$$

It indicates that the phase  $\phi$  can be obtained by solving an ill-posed inverse problem. In view of the piecewise smooth property of  $\phi$  (see Figure 2), we propose the following model for the phase reconstruction problem

$$\min_{\phi} \alpha \|C\phi\|_1 + \frac{1}{2} \sum_{i=1}^m \left\| \begin{bmatrix} RW A_i D_x \\ RW A_i D_y \end{bmatrix} \phi - \begin{bmatrix} s_x^i \\ s_y^i \end{bmatrix} \right\|_2^2, \quad (1.6)$$

where  $\alpha > 0$  is a trade-off constant and  $C \in \mathbb{R}^{l \times n}$  ( $l \geq n$ ) is a tight frame satisfying the orthogonality condition  $C^T C = I$  (see e.g., the monographs [7, 23]). As emphasized in the literature, the tight frame regularization in (1.6) could reconstruct finer details and repeated oscillating patterns of the phase. In essence, the proposed model (1.6) combines the procedures (1.3) and (1.4), and hence saves the additional computation for computing the phase gradients  $\mathbf{s}_x$  and  $\mathbf{s}_y$  (see numerical results reported in Section 4). As we shall show, the model (1.6) can be solved efficiently by the Douglas-Rachford alternating direction method of multipliers (ADMM for short) in [13]. In the following, we will call (1.6) the phase model (see the solid line in Figure 1).

The rest of the paper is organized as follows. In Section 2, we review briefly ADMM. In Section 3, we elaborate on the details of solving the model (1.6) by ADMM. In Section 4, we compare numerically our

proposed phase model with the method in [6] which follows the phase-gradient approach. Finally, some conclusions are drawn in Section 5.

## 2 Preliminaries

In this section, we review the ADMM which will be used to solve the proposed model (1.6). Consider the following convex minimization model with linear constraints and an objective function in separable form:

$$\begin{aligned} \min \quad & \theta_1(x_1) + \theta_2(x_2) \\ \text{s.t.} \quad & B_1x_1 + B_2x_2 = b, \quad x_i \in \mathcal{X}_i, \quad i = 1, 2, \end{aligned} \quad (2.1)$$

where  $\theta_i : \mathbb{R}^{n_i} \rightarrow (-\infty, +\infty]$  ( $i = 1, 2$ ) are proper convex functions;  $B_i \in \mathbb{R}^{m \times n_i}$  are given matrices;  $\mathcal{X}_i \in \mathbb{R}^{n_i}$  are nonempty convex sets;  $b \in \mathbb{R}^m$  is a known vector. Among methods for solving this structured model (2.1), ADMM proposed originally in [13] is a benchmark. Let the augmented Lagrangian function of (2.1) be

$$\mathcal{L}(x_1, x_2, \lambda) = \theta_1(x_1) + \theta_2(x_2) + \lambda^T(B_1x_1 + B_2x_2 - b) + \frac{\beta}{2}\|B_1x_1 + B_2x_2 - b\|_2^2, \quad (2.2)$$

with  $\lambda \in \mathbb{R}^m$  the Lagrange multiplier and  $\beta > 0$  a penalty parameter. Then, the iterative scheme of ADMM can be specified as Algorithm 1 below. For the convergence proof of ADMM for arbitrarily fixed  $\beta > 0$ , we refer to [11–13] for some earlier references; and [16] for its worst-case  $\mathcal{O}(1/n)$  convergence rate. We also refer to [3] and references therein for some efficient applications of ADMM in different areas.

---

### Algorithm 1: Douglas-Rachford alternating direction method of multipliers

---

**Input:** Number of iteration  $N$ , arbitrary  $\beta > 0$ ,  $x_2^0 \in \mathbb{R}^{n_2}$  and  $\lambda^0 \in \mathbb{R}^m$ .

**for**  $k = 1, 2, \dots, N$ , **do**

$$\left| \begin{aligned} x_1^{k+1} &= \arg \min_{x_1 \in \mathcal{X}_1} \mathcal{L}(x_1, x_2^k, \lambda^k) \\ x_2^{k+1} &= \arg \min_{x_2 \in \mathcal{X}_2} \mathcal{L}(x_1^{k+1}, x_2, \lambda^k) \\ \lambda^{k+1} &= \lambda^k - \beta (B_1x_1^{k+1} + B_2x_2^{k+1} - b) \end{aligned} \right.$$

**end**

**Output:**  $(x_1^N, x_2^N)$  as an approximate solution of (2.1) when certain stopping criterion is satisfied.

---

## 3 Implementation of ADMM to the model (1.6)

In this section, we elaborate on how to apply ADMM to solve the model (1.6). For notational convenience, let

$$M_i := \begin{bmatrix} RWA_iD_x \\ RWA_iD_y \end{bmatrix} \quad \text{and} \quad s^i := \begin{bmatrix} s_x^i \\ s_y^i \end{bmatrix},$$

where the operators  $R$ ,  $W$ ,  $A_i$ ,  $D_x$ ,  $D_y$  and the variables  $s_x^i$ ,  $s_y^i$  are as delineated in (1.3)–(1.4). As a result, the model (1.6) reduces to

$$\min_{\phi} \alpha \|C\phi\|_1 + \frac{1}{2} \sum_{i=1}^m \|M_i\phi - s^i\|_2^2. \quad (3.1)$$

By further introducing an auxiliary variable  $u \in \mathbb{R}^n \times \mathbb{R}^n$ , the model (3.1) can be reformulated as

$$\begin{aligned} \min \quad & \alpha \|u\|_1 + \frac{1}{2} \sum_{i=1}^m \|M_i\phi - s^i\|_2^2 \\ \text{s.t.} \quad & C\phi = u. \end{aligned} \quad (3.2)$$

Essentially, the optimization problem (3.2) falls into the form of (2.1) with the following specifications

- $x_1 := \phi$ ,  $x_2 := u$ ,  $\mathcal{X}_1 := \mathbb{R}^n$  and  $\mathcal{X}_2 := \mathbb{R}^l$ ;
- $\theta_1(x_1) := \alpha\|u\|_1$  and  $\theta_2(x_2) := \frac{1}{2} \sum_{i=1}^m \|M_i\phi - s^i\|_2^2$ .
- $B_1 := C$ ,  $B_2 := -I$  and  $b := 0$ .

Consequently, ADMM, i.e., Algorithm 1, can be applied to solve the optimization problem (3.2). We now discuss the resulting subproblems. First, the augmented Lagrangian function of (3.2) can be written as

$$\mathcal{L}(\phi, u, \lambda) = \alpha\|u\|_1 + \frac{1}{2} \sum_{i=1}^m \|M_i\phi - s^i\|_2^2 + \lambda^T(C\phi - u) + \frac{\beta}{2}\|C\phi - u\|_2^2,$$

where  $\lambda \in \mathbb{R}^l$  is the Lagrange multiplier and  $\beta > 0$  is a penalty parameter. Then, we list the  $\phi$ - and  $u$ -subproblem at each iteration of Algorithm 1 for solving (3.2).

- The  $\phi$ -subproblem is

$$\begin{aligned} \phi^{k+1} &= \arg \min_{\phi \in \mathbb{R}^n} \mathcal{L}(\phi, u^k, \lambda^k) \\ &= \arg \min_{\phi \in \mathbb{R}^n} \left\{ \frac{\beta}{2} \left\| C\phi - u^k - \frac{\lambda^k}{\beta} \right\|_2^2 + \frac{1}{2} \sum_{i=1}^m \|M_i\phi - s^i\|_2^2 \right\}. \end{aligned}$$

The minimizer is given by solving the linear system:

$$\left( \beta C^T C + \sum_{i=1}^m M_i^T M_i \right) \phi^{k+1} = C^T(\beta u^k + \lambda^k) + \sum_{i=1}^m M_i^T s^i.$$

Since the tight frame matrix  $C$  satisfies the orthogonality condition  $C^T C = I$ , the  $\phi$ -subproblem reduces to the following positive definite linear system

$$\left( \beta I + \sum_{i=1}^m M_i^T M_i \right) \phi^{k+1} = C^T(\beta u^k + \lambda^k) + \sum_{i=1}^m M_i^T s^i. \tag{3.3}$$

By taking advantage of the sparse structure of matrix  $M_i$  (see [8, 22] for details), the linear system (3.3) can be solved by standard subroutines in numerical algebra. In our numerical tests, we use the conjugate gradient method (see, e.g., [14] for details) to solve this linear system.

- The  $u$ -subproblem is

$$\begin{aligned} u^{k+1} &= \arg \min_{u \in \mathbb{R}^l} \mathcal{L}(\phi^{k+1}, u, \lambda^k) \\ &= \arg \min_{u \in \mathbb{R}^l} \left\{ \alpha\|u\|_1 + \frac{\beta}{2} \left\| C\phi^{k+1} - u - \frac{\lambda^k}{\beta} \right\|_2^2 \right\} \\ &= \text{shrink}_{\frac{\alpha}{\beta}} \left( C\phi^{k+1} - \frac{\lambda^k}{\beta} \right), \end{aligned}$$

where  $\text{shrink}_c(\cdot)$  denotes the well-known shrinkage operator (see [9]). Specifically, the shrinkage operator is defined by

$$\text{shrink}_c(x) := \text{sign}(x) \circ \max\{|x| - c, 0\}, \quad \forall c > 0, \quad x \in \mathbb{R}^l,$$

where “sign” is signum function and “ $\circ$ ” represents the product in componentwise.

Recall the convergence of ADMM has been well established in the literature, see e.g. [11–13, 16]. Therefore, the sequence  $\{\phi^k, u^k, v^k\}$  generated by the above iterative scheme can converge to a solution point of the model (3.2); and consequently the sequence  $\{\phi^k\}$  converges to a solution point of the proposed phase model (1.6).

## 4 Numerical experiments

In this section, we test the performance of the phase model (1.6) and compare it numerically with the phase-gradient model in [6] for the PSF estimation in ground-based astronomy. As indicated by the flowchart in Figure 1, the phase model (1.6) can provide the phase  $\phi$  directly by solving (1.6), while the phase-gradient model first obtains the phase gradients  $\mathbf{s}_x$  and  $\mathbf{s}_y$  by solving an  $l^1$ - $l^2$  model and then solves the linear least squares problem (1.3) by the algorithm in [2] to get the phase  $\phi$  (see [6] for details).

To start the numerical simulation, we first generate the ground truth. Specifically, based on the formula (1.5), we generate the  $m$  frames of low-resolution phase gradients, i.e.,  $s_x^i$  and  $s_y^i$  ( $i = 1, 2, \dots, m$ ), by the following processes

1. Firstly, we generate an  $n$ -by- $n$  true phase  $\phi$  under a certain seeing condition by the method in [1]. Recall that (see Section 1) the seeing condition is generally measured by the ratio  $d/r_0$ , where  $d$  is the diameter of the telescope and  $r_0$  is the Fried parameter.
2. Secondly, the phase gradients, i.e.,  $\mathbf{s}_x$  and  $\mathbf{s}_y$ , are derived from (1.3) by exploiting either Fried geometry [10] or Hudgin geometry [17] to the derivative operators  $D_x$  and  $D_y$ . To simplify the discussion, we only use the Fried geometry [10] in our experiments. As can be seen in [6], both phase and phase-gradient models are applicable to the Hudgin geometry too. Additionally, the zeros mean white noise with a variance  $\sigma$  is further added to both phase gradients. The default setting is  $\sigma = 0.01$  for 128-by-128 phase and  $\sigma = 0.05$  for 256-by-256 phase.
3. Thirdly, by designing a trajectory for the movement of atmospheric turbulence (either linear constant velocity or nonlinear velocity), we can obtain the shift on the phase gradients. That is, we get the motion matrix  $A_i$ .
4. Finally, by confining the phase gradients within the telescope aperture and down-sampling them by a factor of  $\varrho$ , we eventually acquire a sequence of low-resolution phase gradients with  $m$  frames, i.e.,  $s_x^i$  and  $s_y^i$ , ( $i = 1, 2, \dots, m$ ).

Our primary task is to reconstruct the phase  $\phi$  by the sequence of low-resolution phase gradients  $s_x^i$  and  $s_y^i$ ,  $i = 1, 2, \dots, m$ . For the parameters in both models and the penalty parameter  $\beta$  of Algorithm 1, they are tuned manually so as to minimize the relative error (see (4.2)) of the estimated PSF. All the codes for implementing the numerical experiments were written by MATLAB 7.1 and were run on a personal Lenovo laptop computer with Intel(R) Core (TM) 2.30GHZ and 8G memory.

In the following numerical simulations, we separate the tests into two cases in terms of the velocity of moving atmospheric turbulence: linear constant velocity and nonlinear velocity. The parameters for the cases are chosen as follows

- Linear constant velocity:  $\alpha = 10^{-4}$  and  $\beta = 10^{-3}$  for the  $l^1$ - $l^2$  model in phase-gradient model;  $\alpha = 10^{-4}$  and  $\beta = 10^{-4}$  for the model (1.6) in phase model.
- Nonlinear velocity:  $\alpha = 10^{-4}$  and  $\beta = 10^{-4}$  for the  $l^1$ - $l^2$  model in phase-gradient model;  $\alpha = 10^{-4}$  and  $\beta = 10^{-4}$  for the model (1.6) in phase model.

Note that, we employ `pcg` in MATLAB with the tolerance  $10^{-8}$  to solve the subproblems (3.3). The stopping rule for ADMM implementation in solving both models is set as

$$\min \left\{ \frac{\|\mathbf{s}_x^{k+1} - \mathbf{s}_x^k\|}{1 + \|\mathbf{s}_x^k\|}, \frac{\|\mathbf{s}_y^{k+1} - \mathbf{s}_y^k\|}{1 + \|\mathbf{s}_y^k\|} \right\} < 10^{-2}. \quad (4.1)$$

The initial points required by ADMM are all taken as zeros. Figures 3–4 illustrate the reconstructed phases, denoted by  $\tilde{\phi}$ , by the phase-gradient and phase models when the stopping rule (4.1) is reached. Visually, compared to the phase model, the reconstructed phases  $\tilde{\phi}$ 's by the phase-gradient model are over-smoothed and contain fuzzy edges.

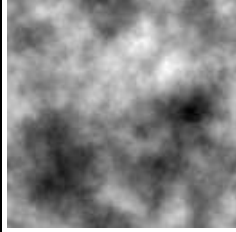
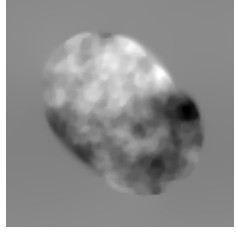
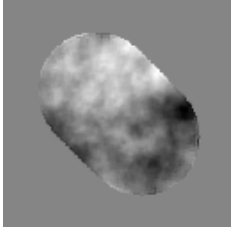
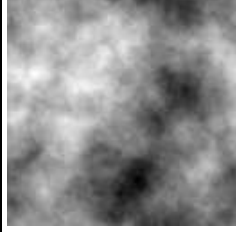
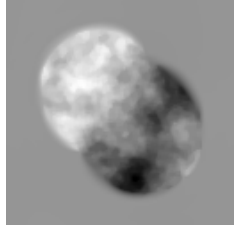
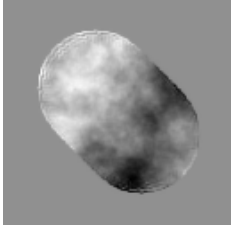
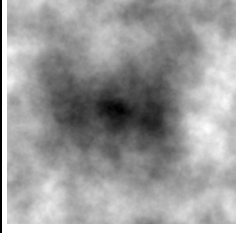
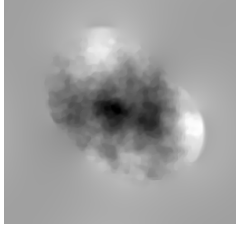
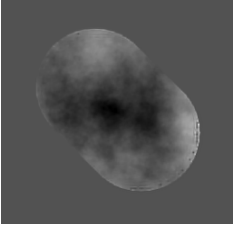
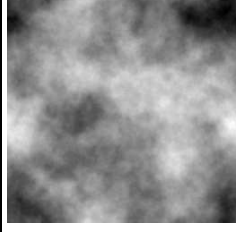
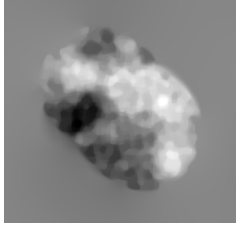
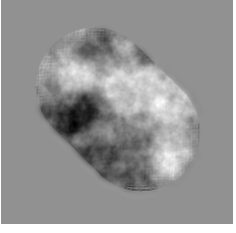
Example	true $\phi$	$\tilde{\phi}_{\text{phase-gradient}}$	$\tilde{\phi}_{\text{phase}}$
E.g. 1: $n = 128$ $m = 16$ $\frac{d}{r_0} = 5$ $\varrho = 4$			
E.g. 2: $n = 128$ $m = 16$ $\frac{d}{r_0} = 50$ $\varrho = 4$			
E.g. 3: $n = 256$ $m = 16$ $\frac{d}{r_0} = 5$ $\varrho = 4$			
E.g. 4: $n = 256$ $m = 16$ $\frac{d}{r_0} = 50$ $\varrho = 8$			

Figure 3. Numerical results of phase reconstruction with the atmospheric turbulence moving in linear constant velocity ( $n$ : size of  $\phi$ ;  $m$ : the number of low-resolution frames;  $d/r_0$ : seeing condition;  $\varrho$ : down-sampling factor).

In order to illustrate the accuracy of the reconstructed phases  $\tilde{\phi}$ , we also compute the PSF at each frame and compare them with the true PSF. Specifically, with a reconstructed phase  $\tilde{\phi}$  at hand, we first compute the corresponding phase at the  $i$ -th frame, i.e.,

$$\tilde{\phi}^i = WA_i\tilde{\phi}, \quad i = 1, 2, \dots, m.$$

Then, by substituting each  $\tilde{\phi}^i$  into (1.2), we get the estimation of PSF at the  $i$ -th frame. We denote the relative error of an estimated PSF by

$$\text{Relative error} = \frac{\|\tilde{k}_i(x, y) - k_i(x, y)\|_2}{\|k_i(x, y)\|_2}, \quad i = 1, 2, \dots, m. \tag{4.2}$$

where  $k_i(x, y)$  is the true PSF at the  $i$ -th frame and  $\tilde{k}_i(x, y)$  is the corresponding estimated PSF. In Figures 5–6, we plot the relative error of the estimated PSF for all frames reconstructed by both models. We see that the relative error of PSF estimated by the phase model is lower than that by the phase-gradient model. Meanwhile, the accuracy of estimated PSF is little affected by the location of frame, i.e., the evolution of relative error with respect to the number of frame has little fluctuation.

In Tables 1–2, we list the number of iterations (“It”) and the computing time in seconds (“cpu”) at each stage of both models. Again, note that the phase-gradient model first reconstructs the phase gradients  $\mathbf{s}_x$  and  $\mathbf{s}_y$ , and then solves the linear inverse problem (1.3) to get the phase  $\tilde{\phi}$ . We see that

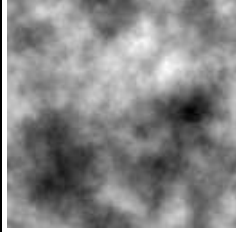
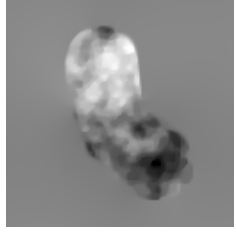
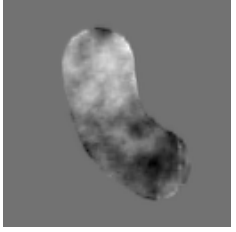
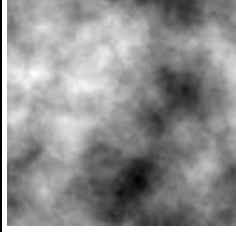
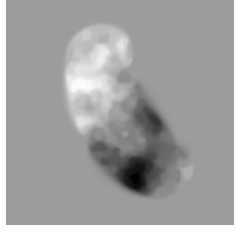

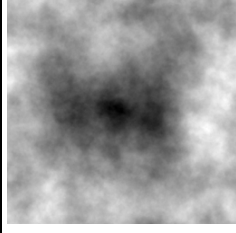
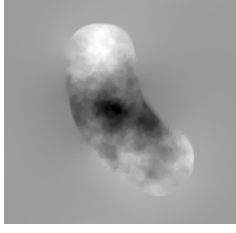
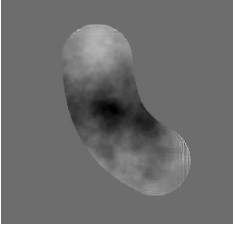
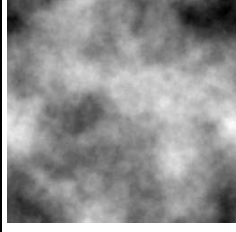
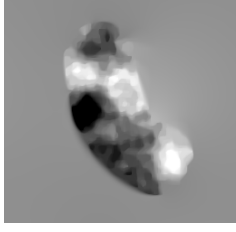
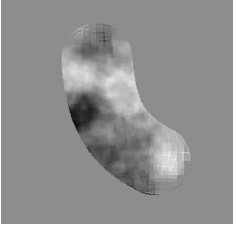
Example	true $\phi$	$\hat{\phi}_{\text{phase-gradient}}$	$\hat{\phi}_{\text{phase}}$
E.g. 1: $n = 128$ $m = 16$ $\frac{d}{r_0} = 5$ $\varrho = 4$			
E.g. 2: $n = 128$ $m = 16$ $\frac{d}{r_0} = 50$ $\varrho = 4$			
E.g. 3: $n = 256$ $m = 16$ $\frac{d}{r_0} = 5$ $\varrho = 4$			
E.g. 4: $n = 256$ $m = 16$ $\frac{d}{r_0} = 50$ $\varrho = 8$			

Figure 4. Numerical results of phase reconstruction with the atmospheric turbulence moving in nonlinear velocity ( $n$ : size of  $\phi$ ;  $m$ : the number of low-resolution frames;  $d/r_0$ : seeing condition;  $\varrho$ : down-sampling factor).

the phase model is more efficient than the phase-gradient model. Moreover, we can draw the following conclusions from these tables:

- The computational cost of both models grows with respect to the size of phase;
- The computational cost is little affected by either the seeing conditions or the movement pattern of atmospheric turbulence;
- Given the same phase, the degree of down-sampling affects the computational cost for both models.

## 5 Conclusions

In this paper, we develop a new model for estimating the point spread function (PSF) in ground-based astronomy. Different from phase-gradient models in the literature, the new model reconstructs the phase directly. We use the tight frame as regularization functional and the Douglas-Rachford alternating direction method of multipliers to solve the new model. Numerical results are reported to show the effectiveness of the new model. For future work, we shall investigate how to estimate PSF engendered by several dominant layers of atmosphere turbulence.



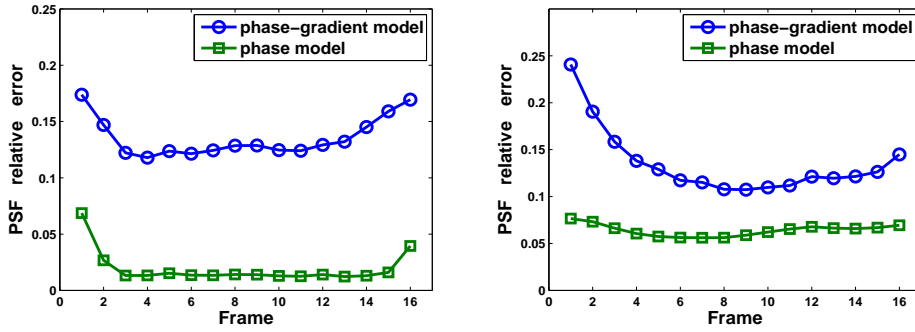


Figure 5 Relative errors of estimated PSF for Examples 2 (left) and 4 (right) in Figure 3.

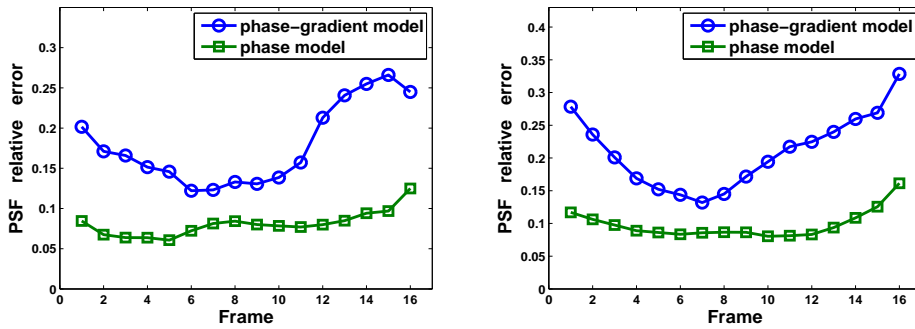


Figure 6 Relative errors of estimated PSF for Examples 2 (left) and 4 (right) in Figure 4.

**Acknowledgements** The first author is supported in part by Hong Kong Research Grants Council (HKRGC) Grant No. CUHK400412, CUHK DAG 4053007, and CUHK FIS Grant 1902036. The second author was supported by Hong Kong Research Grants Council (HKRGC) Grant No. HKBU203311. The authors would like to thank Professor James Nagy and Qing Chu for providing the references [8,22] and the corresponding codes which are very useful for accomplishing this paper.

**References**

- 1 Bardsley J M. Wavefront reconstruction methods for adaptive optics systems on ground-based telescopes. *SIAM J Matrix Anal Appl*, 2008, 30: 67–83
- 2 Bardsley J M, Knepper S, Nagy J G. Structured linear algebra problems in adaptive optics imaging. *Adv Comput Math*, 2011, 35: 103–117
- 3 Boyd S, Parikh N, Chu E, Peleato B, Eckstein J. Distributed optimization and statistical learning via the alternating direction method of multipliers. *Found Trends Mach Learn*, 2010, 3: 1–122
- 4 Chan T F, Shen J. *Image Processing and Analysis: Variational, PDE, Wavelet and Stochastic Methods*. Philadelphia: SIAM, 2005
- 5 Chan T F, Wong C K. Total variation blind deconvolution. *IEEE Trans Image Process*, 1998, 7: 370–375
- 6 Chan R H, Yuan X M, Zhang W X. Point-spread function reconstruction in ground-based astronomy by  $l^1$ - $l^p$  model.

Table 1 Comparison at each stage of phase-gradient and phase models for the examples in Figure 3.

Example	phase-gradient model			phase model	
	for $s_x, s_y$	for $\phi$	for PSF	for $\phi$	for PSF
1	It:12; cpu:1.5	cpu: 3.7	cpu:0.05	It:23; cpu:1.3	cpu:0.05
2	It:14; cpu:1.6	cpu: 4.1	cpu:0.05	It:23; cpu:1.3	cpu:0.05
3	It:12; cpu:4.3	cpu:16.5	cpu:0.17	It:22; cpu:4.1	cpu:0.16
4	It:15; cpu:9.5	cpu:16.4	cpu:0.16	It:25; cpu:7.4	cpu:0.16

Table 2 Comparison at each stage of phase-gradient and phase models for the examples in Figure 4.

Example	phase-gradient model			phase model	
	for $\mathbf{s}_x, \mathbf{s}_y$	for $\phi$	for PSF	for $\phi$	for PSF
1	It:12; cpu:1.1	cpu: 3.4	cpu:0.04	It:22; cpu:0.7	cpu:0.04
2	It:13; cpu:1.3	cpu: 4.2	cpu:0.04	It:21; cpu:0.7	cpu:0.04
3	It:12; cpu:4.1	cpu:14.7	cpu:0.16	It:22; cpu:3.4	cpu:0.16
4	It:14; cpu:8.4	cpu:15.9	cpu:0.16	It:24; cpu:5.7	cpu:0.16

J Opt Soc Amer A, 2012, 29: 2263–2271

- 7 Daubechies I. Ten Lectures on Wavelets. CBMS-NSF Regional Conference Series in Applied Mathematics, Philadelphia: SIAM, 1992
- 8 Chu Q, Jefferies S, Nagy J G. Iterative wavefront reconstruction for astronomical imaging. SIAM J Sci Comput, to appear.
- 9 Donoho D. De-noising by soft-thresholding. IEEE Trans Inform Theory, 1995, 41: 613–627
- 10 Fried D L. Least-squares fitting a wave-front distortion estimate to an array of phase-difference measurements. J Opt Soc Am, 1977, 67: 370–375
- 11 Gabay D, Mercier B. A dual algorithm for the solution of nonlinear variational problems via finite element approximations. Comput Math Appli, 1976, 2: 17–40
- 12 Glowinski R. Numerical Methods for Nonlinear Variational Problems. Springer-Verlag, 1984
- 13 Glowinski R, Marrocco A. Approximation par éléments finis d'ordre un et résolution par pénalisation-dualité d'une classe de problèmes non linéaires, R.A.I.R.O., R2, 1975, 41–76
- 14 Golub G H, Van Loan C F. Matrix Computations. Johns Hopkins University Press, 1996
- 15 Goodman J W. Introduction to Fourier Optics. McGraw-Hill, 1996
- 16 He B S, Yuan X M. On the  $\mathcal{O}(1/n)$  convergence rate of Douglas-Rachford alternating direction method. SIAM J Numer Anal, 2012, 50: 700–709
- 17 Hudgin R H. Wavefront reconstruction for compensated imaging. J Opt Soc Am, 1977, 67: 375–378
- 18 Jefferies S M, Hart M L. Deconvolution from wave front sensing using the frozen flow hypothesis. Opt Express, 2010, 19: 1975–1984
- 19 Jefferies S M, Hart M L, Hege E K, Georges J. Sensing wave-front amplitude and phase with phase diversity. Appl Opt, 2002, 41: 2095–2102
- 20 Lam E Y, Goodman J W. Iterative statistical approach to blind image deconvolution. J Opt Soc Am A, 2000, 17: 1177–1184
- 21 Mugnier L M, Robert C, Conan J M, Michau V, Salem S. Myopic deconvolution from wave-front sensing. J Opt Soc Am, 2001, 18: 862–872
- 22 Nagy J G, Jefferies S M, Q. Chu Q. Fast PSF reconstruction using the frozen flow hypothesis. Proceedings of the Advanced Maui Optical and Space Surveillance Technologies Conference, September 13–16, 2010
- 23 Starck J L, Murtagh F, Fadili J M. Sparse Image and Signal Processing: Wavelets, Curvelets, Morphological Diversity. Cambridge: Cambridge University Press, 2010